Results in Engineering 23 (2024) 102475

Contents lists available at ScienceDirect

Results in Engineering

journal homepage: www.sciencedirect.com/journal/results-in-engineering

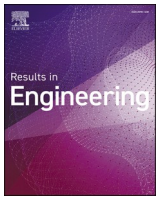

Large eddy simulation-based modeling of cold-air inhalation from nasal cavities to the distal lung: Insights for athlete health and performance

Xinlei Huang [a], Isabella Francis [a], Goutam Saha [a,b], Md. M. Rahman [c], Suvash C. Saha [a,*]

[a] School of Mechanical and Mechatronic Engineering, Faculty of Engineering and Information Technology, University of Technology Sydney, Sydney, NSW, Australia
[b] Department of Mathematics, University of Dhaka, Dhaka, 1000, Bangladesh
[c] Department of Mathematics, Faculty of Science, Islamic University, Kushtia, 7003, Bangladesh

ARTICLE INFO

Keywords:
Computational fluid dynamics
Large eddy simulation
Heat transfer
Thermoregulation
Respiratory tract
Athlete health

ABSTRACT

In cold environments, athletes are frequently susceptible to injuries from inhaling cold and dry air, posing significant health risks. Despite abundant prior research focusing on risk analysis and prevention, the existing body of literature has predominantly focused on heat transfer within lung airways while mainly overlooking the broader respiratory tract. This pioneering study introduces a comprehensive assessment of the entire respiratory system, spanning from the nasal and oral cavities to the larynx, then the trachea, and extending to the 13th generation of lung airways. Employing cutting-edge Computational Fluid Dynamics (CFD) techniques, the investigation operates Large Eddy Simulation (LES) integrated with an algebraic wall-modeled LES subgrid-scale model to simulate heat transfer within the human lung. This approach provides a detailed insight into the complex dynamics of respiratory thermoregulation in cold environments. By offering a comprehensive analysis of the temperature, heat flux, Nusselt number and static pressure profiles throughout the respiratory system, this study fundamentally advances our understanding of the physiological responses of the respiratory system to cold air exposure. These findings have paramount implications for athlete health and performance, shedding light on the complexities of cold-induced respiratory challenges. Moreover, this research lays a solid foundation for developing more effective preventive measures and strategies for optimizing athletic performance in cold weather conditions.

1. Introduction

Participating in athletic activities in cold environments presents athletes with substantial health risks, primarily due to the rapid inhalation of cold and dry air, which can inflict damage on lung tissue. When air is inhaled, it is warmed to the body's core temperature, while exhaled air is cooled, contributing to body heat regulation [1]. This thermoregulatory mechanism of the respiratory system diminishes the temperature disparity between the internal body and the external environment, thus playing a critical role in maintaining bodily homeostasis [2].

Despite the complexity of the human respiratory system and the inherent risks of in vivo interventions, there is an urgent demand for comprehensive research in the domain, particularly concerning the inhalation of cold air [3,4]. Over the past twenty years, the application of CFD has witnessed a remarkable expansion [5], fundamentally altering our comprehension of physiological phenomena across both healthy and pathological conditions [6]. Notably, Shamohammadi et al. [7] undertook a numerical investigation into the thermal dynamics and moisture transport within the upper respiratory tract, analyzing the potential for thermal damage due to heated airflow. Although several studies have examined heat and moisture exchange [8], focusing on the air conditioning functions of the nasal cavity [9,10], evaluating pressure drops within the nasal cavity [11,12], there remains a paucity of information on thermal and inhalational injuries within the pulmonary system [13].

Inhalation injuries, which are clinically complex and rapidly progressing, are commonly categorized into upper and lower airway damages, posing significant challenges within the medical field [14,15]. Such injuries, primarily thermal in nature, are often a result of inhaling steam or hot gases [16] and are a leading cause of burn-related fatalities due to the extensive damage they inflict on lung tissues and the respiratory system [17]. Moreover, many clinical studies have established the connections between inhalation of cold air and core temperature

* Corresponding author.
E-mail address: Suvash.Saha@uts.edu.au (S.C. Saha).

https://doi.org/10.1016/j.rineng.2024.102475
Received 11 January 2024; Received in revised form 31 May 2024; Accepted 25 June 2024
Available online 25 June 2024

changes, cerebral blood flow alteration [18], cardiovascular responses [19], and respiratory symptoms [20]. While the thermodynamic impact on the lower airway post-injury is substantial [21], most preceding studies have predominantly focused on simulating airflow velocities in the upper airways under various respiratory conditions [22,23], leaving a gap in comprehensive lower airway analysis.

The relationship between athlete performance and ambient temperature has been extensively studied, revealing significant impacts across various conditions. Research has established the thermal neutral zone—a temperature range where the body maintains its temperature without additional heat production—as below 28.5 °C, considering lower temperatures as physiologically "cold" [24,25]. Performance variations have been observed with changes in ambient temperatures. For instance, maximal wrist flexion force contraction was more significantly reduced at an air temperature of 5 °C [26]. In sedentary individuals, performance deficits such as impaired drop jump outcomes were noticeable even at mild cooling temperatures like 20 °C, worsening with further cooling [27]. Similar performance decrements were observed in elderly women, where leg extensor power significantly decreased after 45 min of exposure to 15 °C compared to more temperate conditions of 25 °C [28]. However, in climbing-specific tasks performed at 10 °C, maximum voluntary contraction strength of the finger flexor muscles was not adversely affected, and time to task failure actually improved, suggesting varied responses based on the nature of the activity and muscle groups involved [29]. Therefore, an examination of ambient temperatures of 5 and 25 °C on the human respiratory tract is of great importance as they are representative of conditions known to influence athletic performance.

Acquiring a deeper understanding of thermal physiology is essential for enhancing our comprehension of the thermoregulatory mechanisms that strengthen safer and more efficient engagement in outdoor sports [21]. Therefore, this study endeavors to fill this gap by computing the complex dynamics of heat transfer and airflow patterns within a realistically modeled (computed tomography-based) respiratory tract, extending from the nasal cavities to the distal lung. It also explores the complexities of LES turbulence modeling to ensure precise simulation of an athlete's outdoor running conditions, with ambient air temperature maintained at 5 °C and 25 °C and breathing rates set at 60 breaths per minute. By doing so, this research pioneers an in-depth exploration of the multifaceted interaction between heat transfer and airflow within

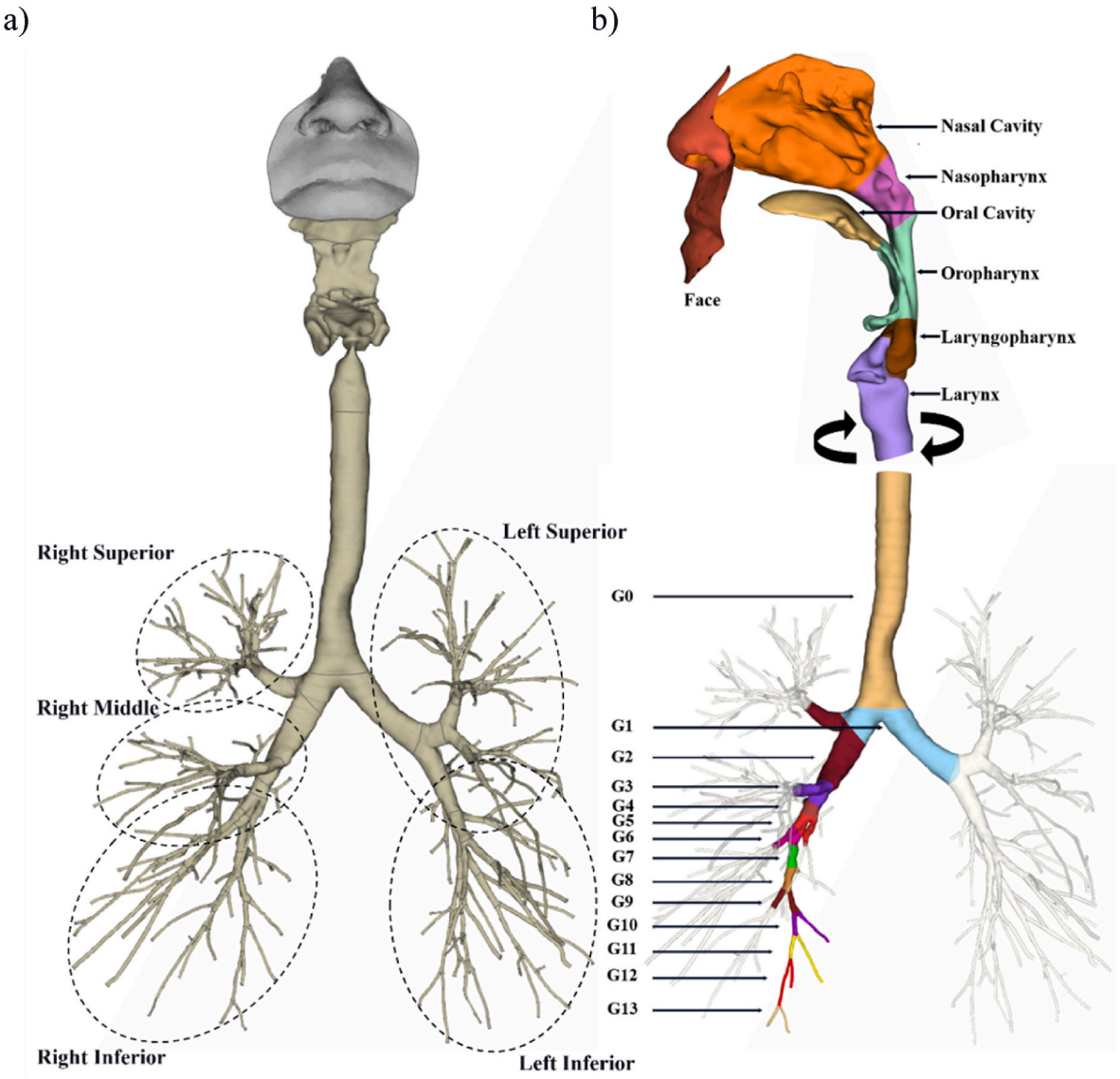

Fig. 1. (a) Three-dimensional visualization of the refined respiratory tract model, featuring the significant lobes (Right superior, middle, and inferior, Left superior and inferior), and (b) Schematic representation of the segmented anatomical components within the respiratory tract from the Nasal cavity to airways of Generation (G) 13, for meshing and simulation convenience.

the respiratory system, clarifying the problems induced by cold exposure. The findings not only enhance our understanding of the cold-induced respiratory challenges faced by athletes but also lay a solid foundation for developing preventive strategies and interventions aimed at optimizing athletic performance in cold conditions.

2. Methodology

2.1. Computational model of the respiratory tract

This investigation entails the development of a computational model for the respiratory tract. The segmentation of highly detailed 3D surface models from CT images is carried out using Mimics Medical 21. Subsequent surface sectioning and enhancement are executed using Geomagic Wrap 2021, followed by post-processing in Siemens NX 12 to ensure the precision of the model. The refined model was then transferred to Ansys for meshing and simulation, resulting in a comprehensive and sophisticated representation of the respiratory tract. For a more detailed exposition of the intricacies of the geometry processing methodology, refer to our prior work [30–32]. The resulting respiratory tract model, as shown in Fig. 1(a), encompasses significant anatomical details. To optimize the convenience of meshing and simulation, the representation of various anatomical components within the respiratory tract was thoughtfully simplified into distinct categories: Nasal cavity, nasopharynx, oral cavity, oropharynx, larynx, laryngopharynx, and airways ranging from Generation (G) 0 to 13, as depicted in Fig. 1(b). Furthermore, ethical approval for this study has been granted by the Human Research Ethics Committees at the University of Technology Sydney, thus authorizing the utilization of human CT scans (ETH23-8670, dated 7 September 2023).

2.2. Governing equations

In this study, the LES [33] technique was employed, with particular emphasis placed on the algebraic wall-modeled LES (WMLES) [34] subgrid-scale (SGS) [35] model. LES represents an advanced computational method distinguished by its unique capability to resolve large-scale turbulent structures while simultaneously parameterizing the more minor unresolved scales, striking a balance between the computational intensity of Direct Numerical Simulation and the efficiency of Reynolds-averaged Navier-Stokes simulations. The incorporation of WMLES within the LES framework epitomizes a more sophisticated and refined strategy for modeling subgrid-scale turbulence, with a primary aim of achieving an unprecedented level of precision in simulating large-scale turbulent structures within complex flows. Crucially, WMLES incorporates a wall function to compute fluid flow characteristics within the near-wall region, a critical zone where boundary layer dynamics significantly impact overall flow patterns. The significance of this innovative methodology becomes particularly pronounced within the context of the study, given the complex internal geometries inherent in the respiratory tract model. By incorporating WMLES, a substantial reduction in the computational workload associated with the exhaustive resolution of near-wall airflow is realized. This strategic integration not only ensures the necessary precision for simulating large-scale turbulent structures but also significantly optimizes the allocation of computational resources. Thus, WMLES plays an important role in enabling comprehensive and exceptionally accurate simulations, particularly in the complex and challenging domain of the respiratory tract.

The principles of continuity, momentum, and energy, derived from the Navier-Stokes equations, are foundational to the understanding of fluid flow dynamics. The continuity equation (Eq. 1) [36], a foundation of mass conservation, ensures that the total mass within a fluid domain remains constant over time, explaining the net rate of mass flow into or out of a control volume. The momentum equation (Eq. 2) [37] models the relations between pressure, viscous forces, and inertial effects, serving as a fundamental framework for understanding the motion of fluid particles. Simultaneously, the energy equation (Eq. 3) [38] captures thermal aspects, including convection, conduction, and heat generation, making it vital for the characterization of temperature variations within turbulent flows.

Continuity equation:

$$\frac{\partial \rho}{\partial t} + \nabla \bullet (\rho \boldsymbol{u}) = 0 \tag{1}$$

Momentum equation:

$$\frac{\partial \rho \boldsymbol{u}}{\partial t} + \nabla \bullet (\rho \boldsymbol{u}\boldsymbol{u}) = -\nabla p + \nabla \bullet (\tau) + \rho \boldsymbol{g} \tag{2}$$

Energy equation:

$$\frac{\partial \rho E}{\partial t} + \nabla \bullet (\boldsymbol{u}(\rho E + p)) = \nabla \left(k_{eff} \nabla T - \sum_j h_j \boldsymbol{J}_j + (\tau_{eff} \bullet \boldsymbol{u}) \right) \tag{3}$$

The eddy viscosity used for the LES is calculated from the optimized algebraic WMLES equations [34], in which the turbulence viscosity is calculated as follows:

$$\upsilon_t = min\left[(\kappa d_w)^2, \left(C_{Smag}\Delta\right)^2 \bullet S \bullet \left\{ 1 - exp\left[-\left(\frac{y^+}{25}\right)^3 \right] \right\} \right] \tag{4}$$

2.3. Discretization scheme

In this investigation, a polyhedral hybrid mesh configuration was employed, illustrated in Fig. 2. The boundary layer within this polyhedral hybrid mesh primarily consists of hexagonal prisms, amounting to 0.21 million cells, while the remaining spatial volume is characterized by irregular polyhedral cells, totaling 7.61 million cells. Consequently, the overall cell count for the entire model reaches 7.83 million cells. Additionally, an optimized non-uniform density mesh design has been integrated to enhance computational efficiency. This design strategically allocates denser node distributions to regions with heightened turbulent intensity [39] and small geometric features. Notably, the mean nodal spacing is tailored to 0.4 mm for the upper airway, 0.35 mm for the trachea and primary bronchi, and further refined to 0.2 mm for the smaller branches of the bronchial tree, extending from G3 to G13. Furthermore, the first boundary layer cell height is set at 0.1 times the local nodal distance, resulting in a dynamically adaptive boundary layer cell thickness throughout the model.

2.4. Model configuration: boundaries and material properties

A comprehensive exposition in Table 1 details the boundary

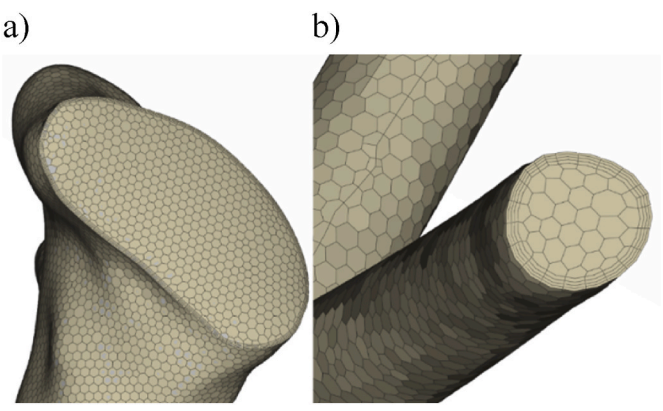

Fig. 2. Mesh configuration illustrating (a) The right nostril inlet with hexagonal prism-based boundary layer mesh and (b) One of the bronchial outlets characterized by irregular polyhedral cells, showcasing the comprehensive spatial meshing strategy for the entire model.

Table 1
Model boundary conditions and material attributes.

Boundary Conditions	Value (Unit)		Ref.
Inlet Velocity	Realistic velocity profile		[40]
Inner wall initial temperature	310.15 (K)		[30]
Outer wall temperature	310.15 (K)		[30]
Outlet pressure	0 (Pa)		[30]
Wall conduction	1 layer shell conduction		[30]
Wall thickness	5 (mm)		[41]
Simulation time step size	1×10^{-5}(s)		–
Simulation time	0.43 (s)		[40]
Material Property	**Value**		**Ref.**
Wall conductivity	0.2 ($Wm^{-1}K^{-1}$)		[42]
Wall density	250 (kgm^{-3})		[43]
Wall specific heat	3886 ($Jkg^{-1}K^{-1}$)		[42]
Air Property	**25 Celsius**	**5 Celsius**	**Ref.**
Air in the airway initial temperature	310.15	310.15 (K)	[30]
Cool air temperature	298.15	278.15 (K)	[30]
Cool air density	1.184	1.270 (kgm^{-3})	[30]
Cool air thermal conductivity	0.025	0.024 ($Wm^{-1}K^{-1}$)	[30]
Cool air dynamic viscosity	1.849×10^{-5}	1.748×10^{-5} (Pa s)	[30]
Cool air specific heat	1007.5	1005.7 ($Jkg^{-1}K^{-1}$)	[30]

conditions and material properties that constitute the basis of this research. The inlet velocity is defined by a velocity profile, an outcome of empirical measurements [40]. This profile faithfully captures the dynamics of incoming air, thus assuring the fidelity of the simulations. In this model, the inner wall temperature is initialized at 310.15 K to match physiological conditions. Similarly, the outer wall remains unwavering at a constant temperature of 310.15 K, fostering a thermally stable environment within the computational domain. The outlet pressure is calibrated to 0 Pa relative to the surrounding atmosphere, mirroring an open boundary condition. To accommodate the dynamics of wall conduction, the model incorporates a one-layer shell conduction methodology, adjusting to a wall thickness of 5 mm. The one-layer shell conduction model, a practical and effective approach for simulating heat transfer through solid structures, simplifies the computational framework. This model conceives the solid structure as a monolithic layer characterized by uniform thermal properties, encompassing thermal conductivity, specific heat, and density. It operates under the assumption that temperature variations predominantly occur in a single direction, perpendicular to the surface. This simplification is optimally suited for scenarios where heat transfer within the solid materializes in a relatively uniform fashion, affording a reduction in computational complexity. The finesse of this model alleviates the imperative for fine-grained meshing and complex calculations. The simulation spans 0.43 s, aligning precisely with the physiological inhalation period, as depicted in Fig. 3.

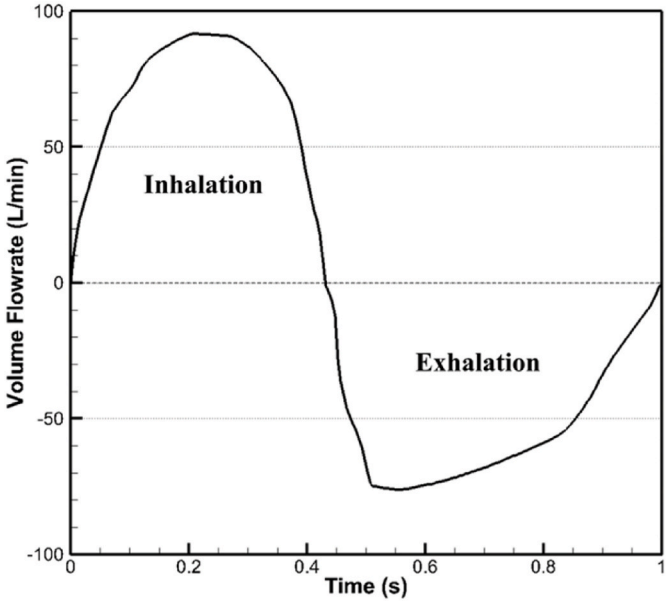

Fig. 3. Variation in volume flow rate over one complete breathing cycle, sourced from Wedel et al. [40].

2.5. Validation

The methodology forming the basis of this study has previously undergone rigorous numerical validation, as documented in our prior research [30]. For further verification, we conducted a mesh independence analysis to confirm the robustness and reliability of our computational simulations. This process entailed systematic mesh refinement with two sequential stages, each using a refinement factor of 1.5, resulting in meshes with 3.8, 5.1, and 7.8 million cells, respectively, representing coarse, medium, and fine levels of resolution.

Fig. 4 (a, b) serves as a graphical representation of the simulation results, illustrating the convergence behavior of the volume-averaged static temperature and area-weighted average surface heat flux within the respiratory tract. It is evident that the static temperature and heat flux exhibited minimal fluctuations in their profiles once the total cell count exceeded 5 million cells. This observation strongly supports the adequacy of the 7.8 million cell mesh employed in our investigation.

The investigation extended to analyzing several time-averaged area-weighted average (TAAWA) parameters of the trachea derived from simulations at different mesh resolutions. Table 2 presents the computational outcomes, where the residuals among the coarse, medium, and fine mesh results are also computed. The findings reveal that variations across the meshes fall within an acceptable tolerance range, with the majority of the values' residual falling within 5 %, indicating mesh convergence for the values.

Finally, the study quantified the total flow percentage across various lung lobes, using the fine mesh for detailed flow dynamics. The results were then compared with existing CFD studies to benchmark our findings against established data, as presented in Table 3. As can be seen from the comparison, the present CFD results fall within the range of previous data.

2.6. Verification

The current investigation incorporates additional experimental validation to fortify the robustness of the simulation results. Specifically, the temperature profile of the trachea, as measured in vivo [44] served as the benchmark for the verification of the simulated temperature field, depicted in Fig. 4(c). We compared the point temperature profile, obtained from experimental measurements during a patient's breathing cycle, against the area-averaged wall temperature from our current study's simulation set at 298.15 K ambient temperature. As shown in Fig. 4(d), upon normalization, the temperature profiles demonstrated a similar trend, affirming the simulation's accuracy and realism. Moreover, an assessment involving the calculation of the total flow percentage in lung lobes is undertaken, which is subsequently compared to previously documented experimental data, as presented in Table 3.

The comparative analysis above reveals a consistency between the outcomes generated by the current simulation and the established range derived from experimental data. This alignment ensures the credibility of the present simulation methodology and accentuates the real-world applicability and reliability of the simulation outcomes.

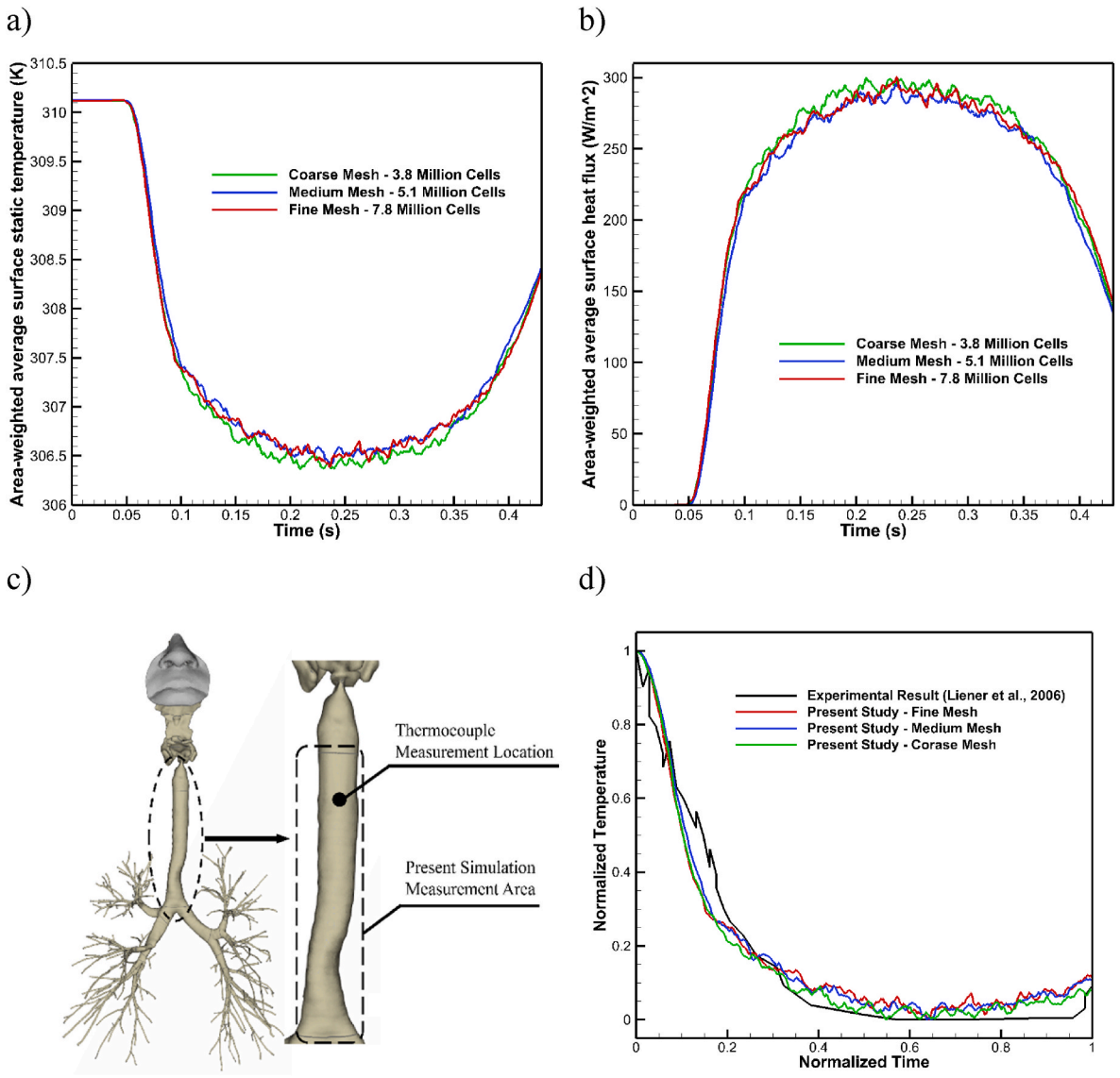

Fig. 4. Validation and verification graphs showing a) convergence behavior of volume-averaged static temperature within the respiratory tract, b) convergence behavior of area-weighted average surface heat flux of the trachea, c) illustration of the location where the in vivo measurement [44] and the present numerical results were obtained, and d) normalized tracheal temperature changes during inhalation between previous in vivo measurement [44] and present numerical simulation.

Table 2
Validation of simulation results through mesh independence study on several TAAWA parameters of the trachea.

Parameter Name	Coarse	Medium	Residual (C-M)	Fine	Residual (M-F)
Surface heat flux	215.640	208.367	3.43 %	213.057	2.23 %
Surface static temperature	307.416	307.508	0.03 %	307.474	0.01 %
Air temperature	305.185	305.251	0.02 %	305.087	0.05 %
Wall-air temperature difference	2.231	2.257	1.16 %	2.387	5.60 %
Heat transfer coefficient	96.656	92.331	4.58 %	89.257	3.39 %
Nusselt number	34.796	33.239	4.58 %	32.133	3.38 %

Table 3
Validation of simulation results through comparative analysis with previous experimental and CFD data.

Total Flow (%)	Previous Experiments		Previous CFD	Present CFD
Regions	Cohen et al. [45]	Horsfield et al. [46]	Islam et al. [47]	value at time step 0.31s
left superior lobe	15.9	20.5	23.38	21.22
left inferior lobe	23.9	24.9	21.82	25.12
right superior lobe	18.2	21.7	21.03	17.6
right middle lobe	9.6	9.6	9.953	11.16
right inferior lobe	32.4	23.2	23.95	24.9
Left Lung	39.8	45.4	45.2	46.34
Right Lung	60.2	54.6	54.93	53.66

3. Results and discussion

3.1. Airway volume temperature

The airway volume temperature, denoting the volume-weighted averaged static temperature, provides a comprehensive perspective on the spatially averaged temperature dynamics across the entire respiratory tract. In theory, the air within the airway initiates at a temperature of 310.15 K. However, as the airway inhales the cooler ambient air at 298.15 and 278.15 K, an anticipated decline in the average temperature ensues. The graphical depiction in Fig. 5 presents the alterations in volume-weighted average temperature throughout the respiratory tract during the inhalation phase. Upon closer examination of the graph, a discernible pattern emerges. Initially, the average temperature experiences a consistent decline within the first 0.1 s, characterized by a rate of approximately 50 K/s and 140K/s for inhaling cool air at 298.15 and 278.15 K, respectively. Subsequently, the average temperature undergoes a gradual transition from this descent, reaching its minimum at 303.8 K and 292.9 K between 0.1 and 0.4 s. The subsequent increase in average temperature beyond 0.4 s culminates in a final reading of 305.9 K and 298.3 K at the conclusion of the inhalation phase. These observations provide invaluable insights into the temporal evolution of average temperature within the respiratory tract during the inhalation process.

In support of the insights presented in Fig. 5, a series of visualizations of 298.15K-air-inhalation simulation offers a detailed perspective on the dynamic thermal transformations occurring within the upper airway. In Fig. 6, a visual representation captures the temperature contours within the central cross-sectional plane of the upper airway, extending from the nasal region to the trachea. This portrayal focuses on the critical time interval from 0.02 to 0.07 s (Fig. 6 a to f). Complementing this, Fig. 7 offers an in-depth depiction of velocity streamlines color-coded according to the volume temperature. This visual representation encompasses a broader temporal spectrum, ranging from 0.03 to 0.43 s.

Evidently, the surge of cold air initiates a phase of swift thermal adaptation within the upper airway. However, what unfolds is an intriguing transformation as the cold air continues its journey through the upper airway. The temperature gradually converges to a state of equilibrium, notably discernible at various anatomical locations, such as the nostril inlet registering at 298 K and the nasopharynx at 302 K, as observed from 0.13 s to 0.38 s in Fig. 7 (c to e). This convergence of temperature levels reflects the dynamic interaction of heat exchange within the respiratory tract, where the most conspicuous temperature gradient occurs at the interface between the cold ambient air and the warmer lung air, while the remaining regions exhibit diminished temperature gradients. As the cold air reaches the outlets of the modeled airway, the entire lung volume attains a state of relative equilibrium, mirroring the horizontal volume temperature profile spanning from 0.1 s to 0.35 s in Fig. 5. This equilibrium highlights the remarkable efficiency of heat exchange in the respiratory tract, resulting from multiple factors, including the steadfast exterior wall temperature, relatively stable incoming air velocity during mid-inhalation, and the combined influence of Newton's law of cooling and Fourier's law of heat conduction. Approaching the conclusion of the inhalation phase, the airflow velocity diminishes, and at multiple locations, airflow patterns exhibit backflow and turbulence, leading to the upward transport of warmed air, as visually depicted in Fig. 7 (f). This circulation of warmer air from deeper regions of the tracheobronchial tree into the respiratory tract outlets corresponds to an increase in volume temperature, reflecting the temperature profile between 0.35s and 0.4s in Fig. 5. For a more comprehensive understanding of the influence of turbulence on local heat distribution, we delve into a detailed discussion in Section 3.6.

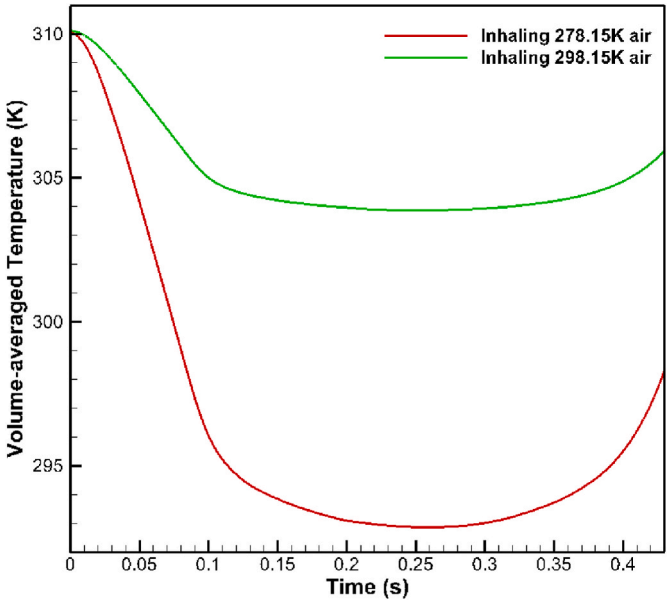

Fig. 5. Temporal evolution of volume-weighted average temperature in the respiratory tract when inhaling air at 298.15 and 278.15 K.

3.2. Airway wall surface temperature

The airway wall surface temperature serves as an interface between the respiratory air and the adjacent wall. In the present study, the human airway wall is modeled as a 5 mm thick, single-layered shell initially maintained at 310.15 K. The inhalation of cooler external air at 298.15 K and 278.15 K initiates a dynamic heat transfer process influenced by conduction and convection mechanisms. According to thermodynamic principles, this process should lead to a decrease in wall surface temperature during inhalation.

Fig. 8 graphically illustrates the dynamic variations in wall surface temperature throughout the inhalation phase. Specifically, Fig. 8 (a) offers insights into oscillations in the overall area-weighted average surface static temperature encompassing both the upper and lower airways. Notably, the airway wall surface temperature undergoes a significant reduction from 0.05 to 0.1 s, reaching its minimum values between 0.2 and 0.25 s. This decline is followed by a pronounced ascent from 0.35 to 0.43 s, shaping a symmetrical "U" trend. This dynamic temperature variation can be attributed to the swift influx of cold air at inhalation initiation, detailed in Figs. 6 and 7, causing a rapid temperature decrease in the upper airway. The subsequent temperature rise is attributed to several factors, including the constant exterior wall surface temperature, changes in airflow velocity, extended air-wall contact area, and heat exchange mechanisms, collectively contributing to gradual wall warming.

Fig. 8 (b), (c) and (d) offer a detailed portrayal of the fluctuations in area-averaged surface static temperature within the lung generations of the lower airway. Notably, two distinct clusters of wall temperature profiles emerge. The first cluster encompasses generations from G0 to G5, where temperatures exhibit large temperature drops. The second cluster comprises generations G9 to G12, where temperatures experience minimal variations. The observed trend reveals a compelling aspect of the lower airway's thermal dynamics. As air journeys deeper into the lungs, it tends to undergo progressive warming due to heat exchange processes. This gradual warming results in minimal temperature changes in the later lung generations. However, generations 6 and 7 present a unique scenario. These sections of the lower airway exhibit significant temperature fluctuations, deviating from the overall trend. This intriguing behavior can be attributed to the airflow dynamics within these specific lung generations. Here, turbulence and backflow phenomena come to the forefront as influential factors. Turbulent airflow is characterized by erratic velocity variations, which inherently affect temperature profiles. Consequently, generations 6 and 7, where

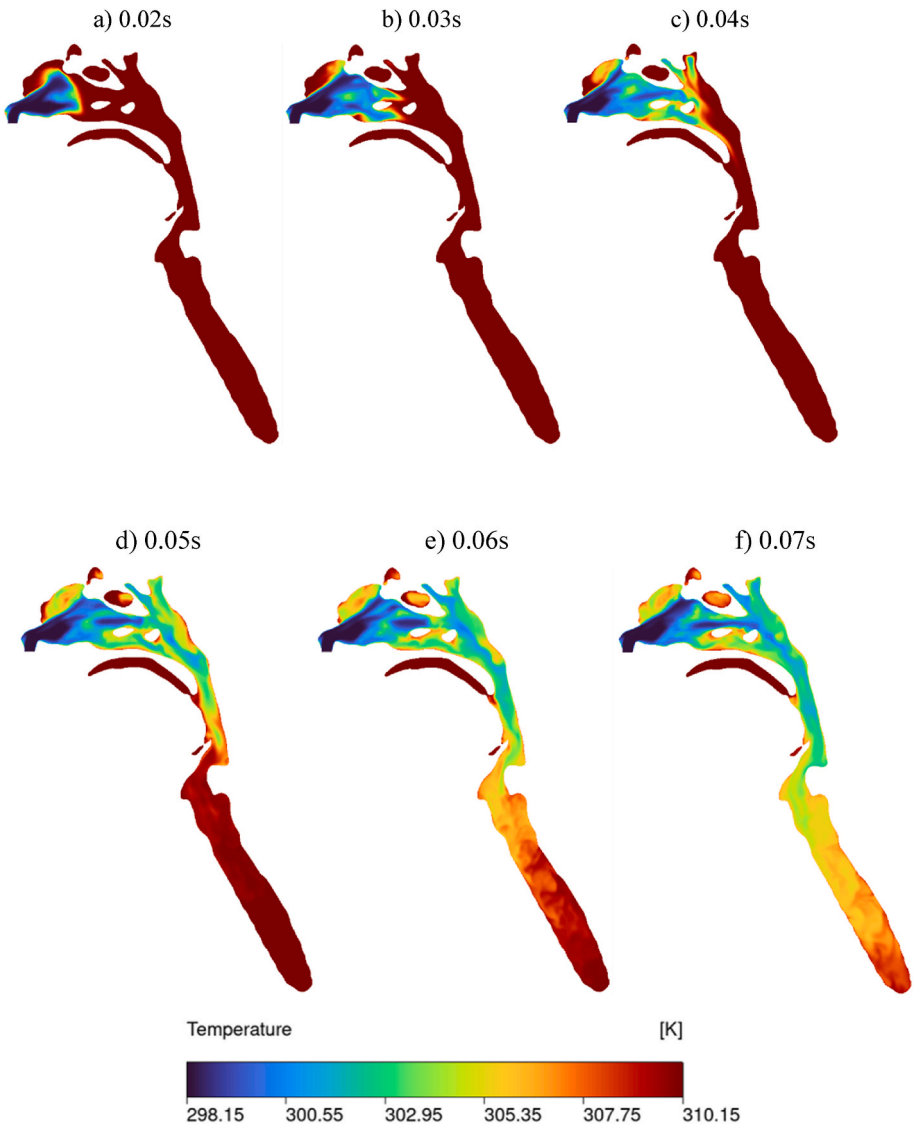

Fig. 6. Temperature (K) contour within the central cross-sectional plane of the upper airway from 0.02 to 0.07 s in the 298.15 K air inhalation simulation, illustrating dynamic thermal changes.

turbulence is pronounced, display noteworthy temperature fluctuations. In contrast, generation 8 represents a distinctive case, where the temperature variations are notably subdued.

Fig. 8 (e) and (f) focuse on the area-averaged surface static temperature within the upper airway regions. This segment reveals a rapid decrease in nasal cavity wall temperature. When inhaling air temperature at 298.15K, the nasal cavity wall temperature dropped to 299 K within 0.05 s and subsequently rose to 300.5 K by the end of the inhalation phase. In stark contrast, the wall temperature of the oral cavity remains stable at 310 K throughout inhalation. Temperature variations in other regions present a similar pattern, each maintaining a consistent temperature difference from the others. This phenomenon arises from thermal conduction and convection interactions within the system. As cooling air descends through the respiratory system, heat is transferred from the wall to the surrounding air, consequently elevating the air temperature. This process diminishes the temperature contrast between the downstream regions, aligning the wall temperature profiles with the anatomical hierarchy, from the upper airway to the lower areas.

3.3. Airway wall surface heat flux

Surface heat flux represents heat transfer per unit area at the air-wall interface, influenced by the heat transfer coefficient and temperature disparities. Fig. 9 comprehensively portrays simulated wall surface heat flux during the inhalation of cool air at 298.15 K and 278.15 K. In Fig. 9 (a), the area-weighted average surface heat flux in the upper and lower airways undergoes a significant reduction from 0.05 to 0.1 s, followed by a peak between 0.2 and 0.25 s and a swift decline from 0.35 to 0.43 s, resulting in a symmetrical "n" pattern. The upper, lower, and entire airways peak at 260, 230, and 240 W/m^2 for 298.15 K-air inhalation and 720, 650 and 670 W/m^2 for 278.15 K-air inhalation, respectively. In Fig. 9 (b), (c) and (d), oscillations in area-averaged surface heat flux within lower airway generations are detailed. Two distinct clusters have emerged, namely G0-G5 and G9-G12, analogous to those observed in Fig. 8 (c) and (d). Notably, G13 diverges due to limited model representation, reducing exposure to cold air, elevating temperatures, and reducing heat flux. G6 and G7 exhibit noticeable fluctuations, while G8 displays modest variation. The initiation point of wall temperature decline and heat flux increase corresponds with anatomical order, influenced by descending cold air introducing temperature gradients, thereby affecting wall temperature and surface heat flux. Fig. 9 (e) and (f) present fluctuations in area-averaged surface heat flux within the upper airway. As can be seen in the 298.15 K-air inhalation profile, a rapid surge occurs in the nasal cavity, reaching 875 W/m^2 in 0.05 s and

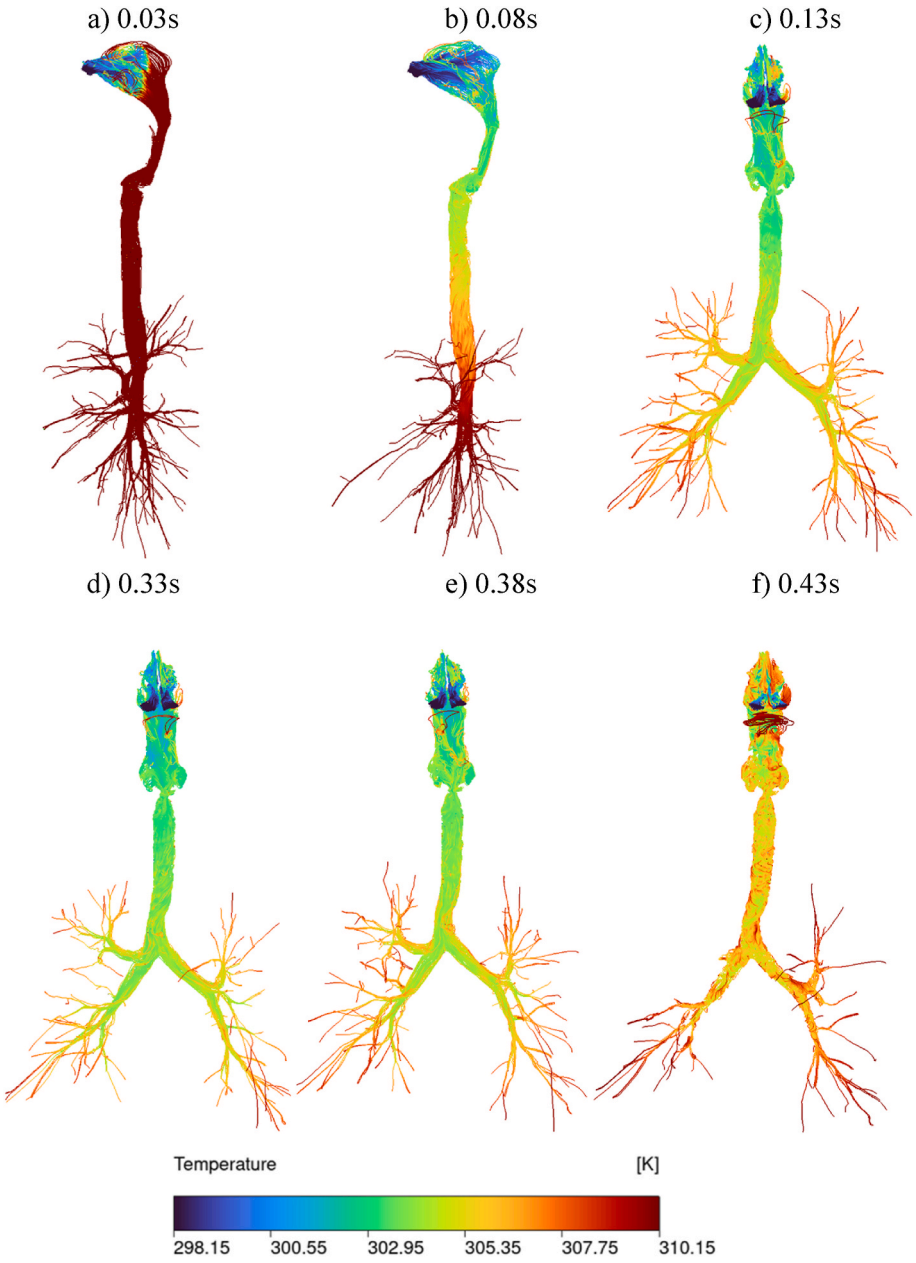

Fig. 7. Velocity streamlines color-coded according to volume temperature in the upper airway from 0.03 to 0.43 s in the 298.15 K air inhalation simulation, revealing the thermal adaptation processes.

gradually subsiding to 775 W/m^2 in 0.4 s. Conversely, the oral cavity maintains low flux, consistently below 25 W/m^2. Other regions exhibit parallel patterns with consistent difference, with peak heat flux values of 300, 350, 400, and 430 W/m^2 in the oropharynx, nasopharynx, laryngopharynx, and larynx, respectively.

3.4. Nusselt number

The TAAWA Nusselt number of the lower airway can then be calculated by using the TAAWA of the surface heat flux, multiplied by the radius of the airway [48], and then dividing by the TAAWA wall-air temperature difference and the thermal conductivity of the air:

$$Nu = \frac{QL}{\Delta T k_{air}} \tag{5}$$

The Nusselt number for each airway generation during inhalation of air at 278.15 K and 298.15 K is shown in Table 4. It is apparent that the airway generation has a significant impact on the convective heat transfer. The observed trend indicates that larger airway radii are associated with higher Nusselt numbers, a consequence of the increased contact surface for heat exchange between the airway wall and the inhaled air. Specifically, G0 exhibits the highest Nusselt numbers for both inhalation temperatures, which suggests that the proximal airways are more effective in heat transfer compared to the distal ones.

As the airway generations progress, there is a notable decrease in the Nusselt number. This reduction can be attributed to the decreasing airway radius, which diminishes the efficacy of convective heat transfer due to the reduction in the surface area available for heat exchange. However, the Nusselt number is not purely a function of airway size; the temperature difference between the wall and the air plays a vital role. The greater temperature gradient observed when inhaling 278.15 K air, as compared to 298.15 K, should enhance the convective heat transfer, leading to a higher Nusselt number. This is reflected in the data, where, across all generations, the Nusselt numbers are consistently higher for

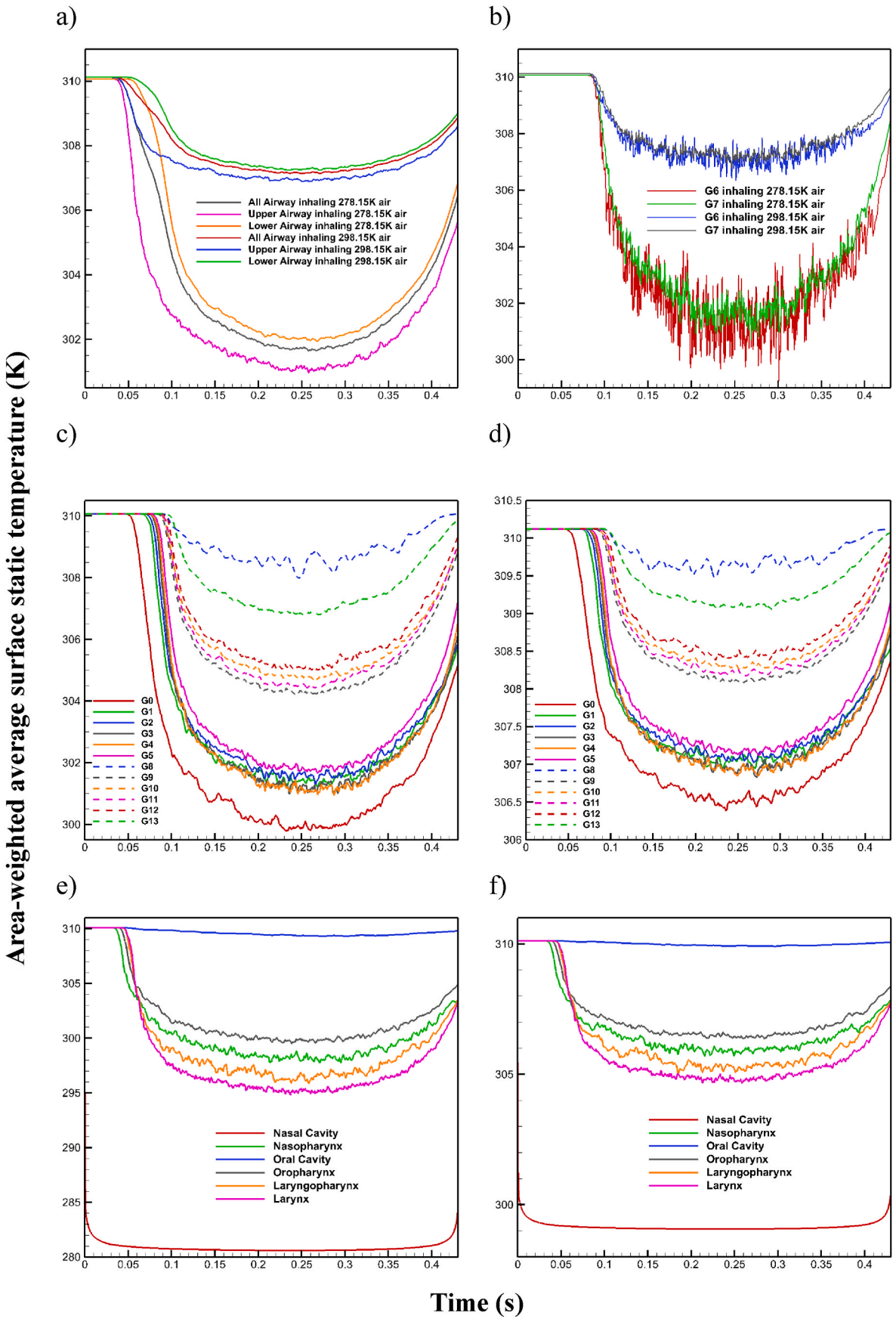

Fig. 8. Temporal changes in airway wall surface temperature (K): (a) Upper and lower airway at 278.15 and 298.15 K, (b) G6-G7 at 278.15 and 298.15 K, (c) Lower airway regions at 278.15 K, (d) Lower airway regions at 298.15 K, (e) Upper airway generations at 278.15 K, and (f) Upper airway generations at 298.15 K.

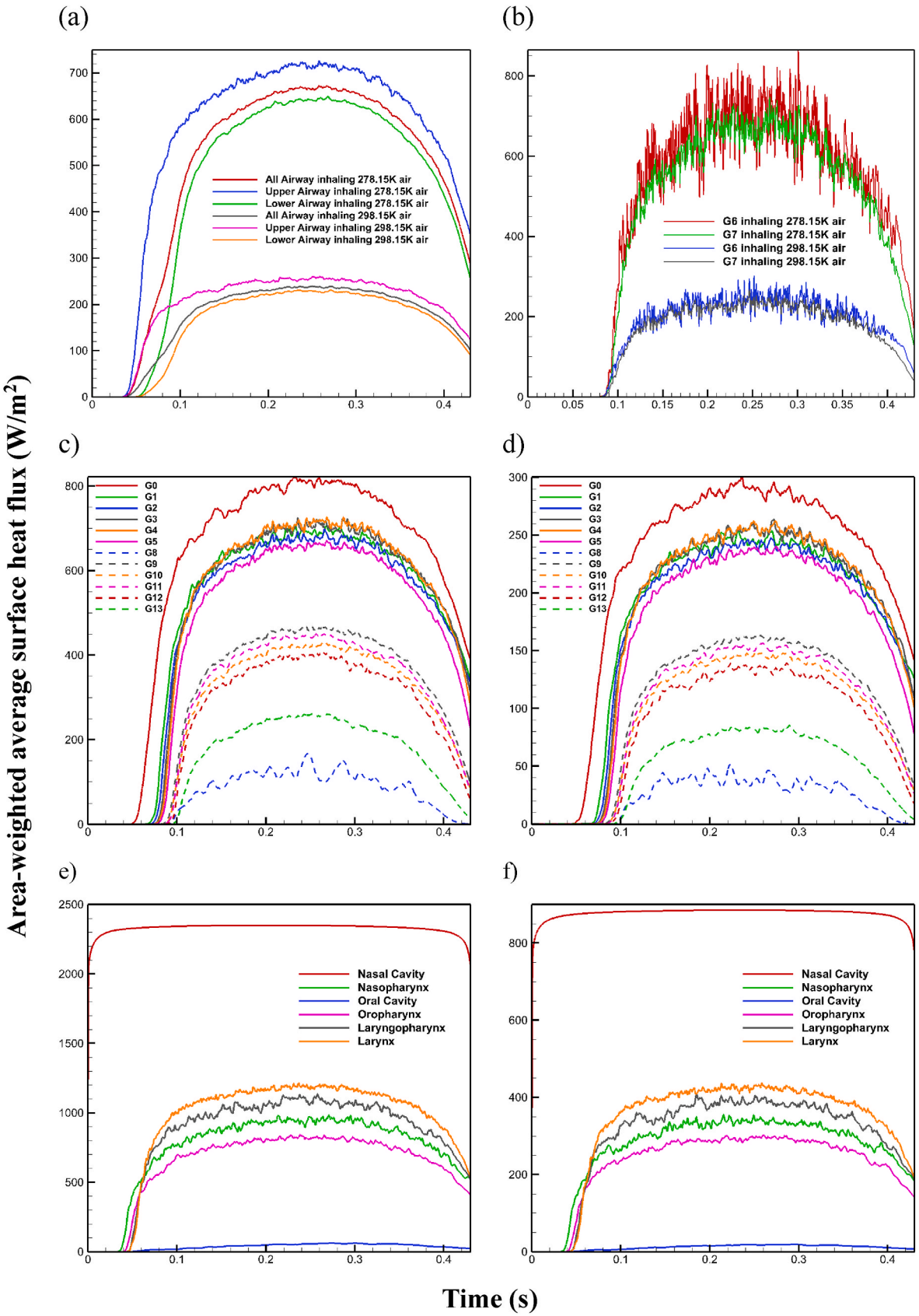

Fig. 9. Temporal changes in wall surface heat flux (W/m^2): (a) Upper and lower airway at 278.15 and 298.15 K, (b) G6-G7 at 278.15 and 298.15 K, (c) Lower airway regions at 278.15 K, (d) Lower airway regions at 298.15 K, (e) Upper airway generations at 278.15 K, and (f) Upper airway generations at 298.15 K.

Table 4
TAAWA Nusselt number and reverent parameters of each airway generation when inhaling 278.15 and 298.15 K cool air.

Generation	Airway Radius (m) [49]	TAAWA wall heat flux ($W•m^{-2}$) (298.15 K)[a]	TAAWA wall heat flux ($W•m^{-2}$) (278.15 K)	TAAWA wall-air temperature difference (K) (298.15 K)	TAAWA wall-air temperature difference (K) (278.15 K)	TAAWA Nusselt number (298.15 K)	TAAWA Nusselt number (278.15 K)
0	0.00900	213.06	594.38	2.39	6.41	32.13	34.75
1	0.00610	173.90	488.76	2.86	7.74	14.85	16.05
2	0.00415	169.02	473.78	2.92	7.93	9.62	10.33
3	0.00280	175.27	489.07	2.85	7.74	6.90	7.38
4	0.00225	175.22	489.69	2.85	7.73	5.54	5.94
5	0.00175	158.99	446.43	3.05	8.27	3.65	3.94
6	0.00162	160.13	459.51	3.03	8.11	3.42	3.82
7	0.00149	48.83	428.85	3.17	8.49	0.92	3.13
8	0.00136	22.49	70.18	4.75	12.99	0.26	0.31
9	0.00122	102.60	295.98	3.75	10.16	1.34	1.48
10	0.00109	92.33	267.15	3.88	10.52	1.04	1.15
11	0.00096	96.56	280.29	3.83	10.35	0.97	1.08
12	0.00083	83.46	246.03	3.99	10.78	0.69	0.79
13	0.00070	47.42	147.19	4.44	12.02	0.30	0.35

[a] Data when inhaling air at 298.15 K.

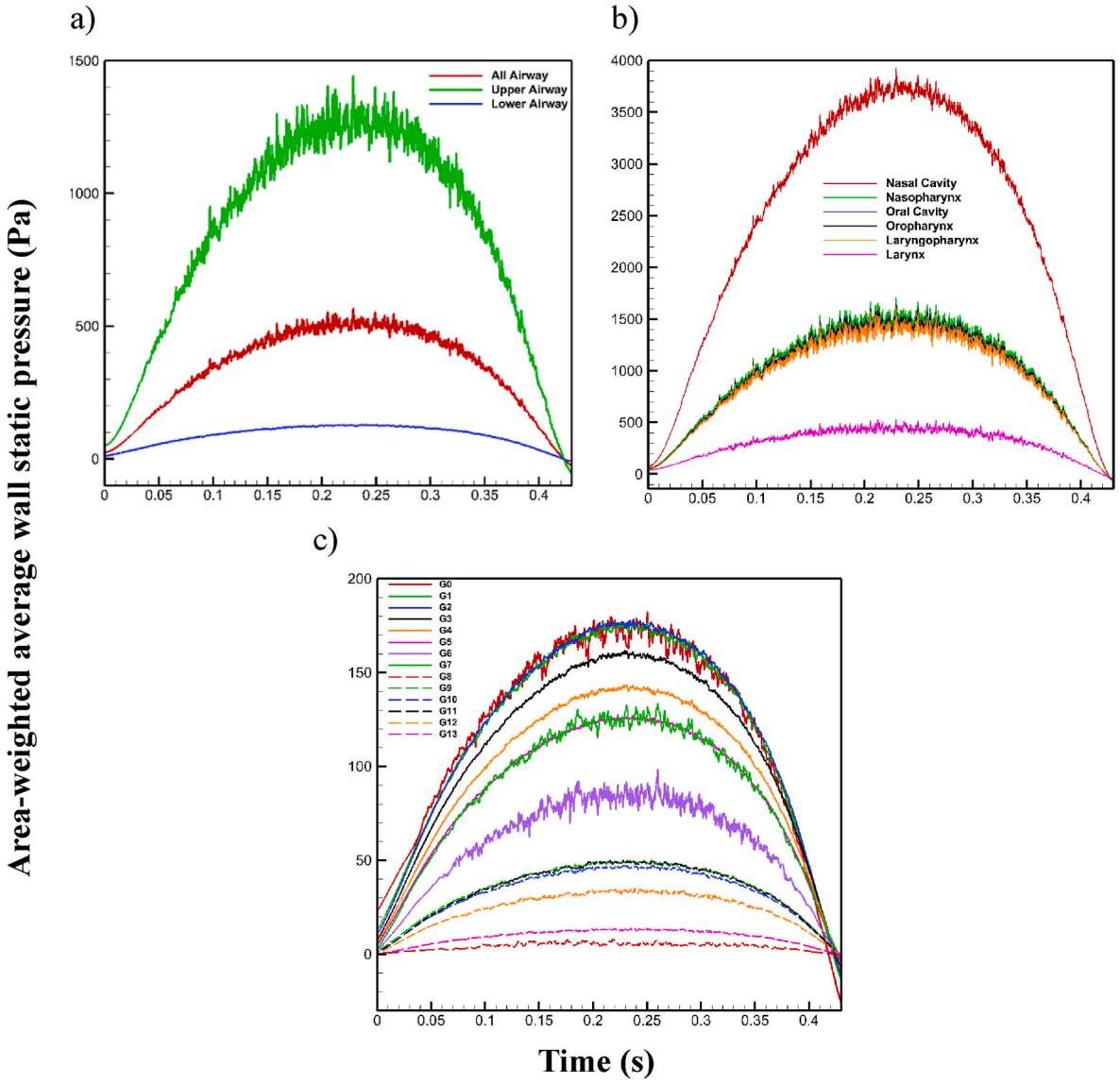

Fig. 10. Area-weighted average wall static pressure (Pa) profiles during inhalation for (a) the upper and lower airways, (b) within upper airway regions, and (c) within the lower airway generations.

278.15 K inhalation.

Notably, at G7, there is an anomaly where the wall heat flux at 298.15 K drops significantly, resulting in a Nusselt number that is notably lower than expected in comparison to adjacent generations. This anomaly may be indicative of a physiological or geometric factor unique to this generation that affects heat transfer. For the smallest airways, Generations 8 through 13, the Nusselt numbers are the lowest across all generations. This observation aligns with the theoretical understanding that reduced surface area in smaller airways leads to diminished heat exchange. Additionally, it may be partly attributable to the limitations inherent within the model. Moreover, the temperature difference for these generations is the greatest, which implies that while the heat transfer is inherently less efficient due to smaller radii, the temperature gradient is sufficiently large to maintain a finite, though small, level of convective heat transfer.

3.5. Static pressure

The force exerted by the air against the airway wall, whether the air remains static or moves with a constant velocity parallel to the surface, is characterized by the area-weighted average wall static pressure. This metric encapsulates the normal force per unit area imparted onto the airway wall by the air and naturally exhibits dynamic variations associated with changing air inflow velocities. A comprehensive representation of the simulated area-weighted average wall static pressure for each region during inhalation is provided in Fig. 10. Note that the pressure profile for the 298.15 K-air inhalation simulation is exclusively presented, as variations in temperature do not significantly affect the pressure field. Fig. 10 (a) shows a holistic view of the averaged static pressure encompassing the upper, lower, and entire airway. Notably, significantly elevated and oscillatory static pressure is experienced by the upper airway, with a surge to 1400 Pa within the brief interval of 0.2–0.25 s. In contrast, the lower airway maintains relatively constant and subdued static pressure, consistently remaining below 150 Pa throughout the inhalation phase. The overall trajectory of the pressure profile resembles a smooth arch, commencing with a swift ascent from 0 Pa to its zenith, followed by an equally rapid descent back to 0 Pa, mirroring the initial ascent pattern. Fig. 10 (b) focuses on the fluctuations in wall static pressure within the upper airway. Notably, the highest pressure is experienced by the nasal cavity, reaching a peak of 3800 Pa. In contrast, the larynx registers the lowest pressure, consistently remaining below 500 Pa throughout the entire inhalation process. Pressure profiles for the remaining regions exhibit a closely aligned pattern, with maximum values falling from 1450 to 1600 Pa. This is by Bernoulli's principle, which postulates that as the velocity of a fluid increases within a flow, the pressure decreases, assuming constant fluid density. The Venturi effect, a specific case of Bernoulli's principle, manifests when a fluid traverses a constricted conduit section. In the context of the respiratory system, this constriction corresponds to the vocal cords within the larynx. As fluid velocity escalates within this confined region, the pressure proportionately diminishes, thus explaining the lowest surface static pressure within the larynx among the upper airway regions.

Fig. 10 (c) illustrates the wall static pressure dynamics within the lower airway. In stark contrast to the clustering observed in temperature and heat flux profiles, the pressure patterns within each region reveal a more evenly distributed configuration. The maximum pressure change is experienced by the trachea, peaking at 180 Pa between 0.2 and 0.25 s and declining to −30 Pa at the conclusion of the inhalation phase. Conversely, minimal pressure variation is displayed by G8 and G13, consistently maintaining levels between 0 and 10 Pa throughout the inhalation process. Notably, among the lower airway regions, elevated fluctuations are exhibited by G0, G6, and G7, a phenomenon also observed in the temperature and heat flux profiles. These fluctuations in pressure, especially within G0, are primarily ascribed to the presence of turbulent airflow, as substantiated by Figs. 11 and 12. The erratic velocity variations of turbulent flows are intrinsically linked with pressure fluctuations. Regions characterized by high fluid velocity tend to register lower pressures, while areas characterized by lower fluid velocities correlate with higher pressures, in accordance with Bernoulli's principle. A notable correspondence with the temperature and heat flux profiles is the alignment of surface static pressure profiles, which, despite some irregularities, are generally found to adhere to the anatomical sequence from head to toe. The inhalation process commences with the diaphragm's contraction and the thoracic cavity's expansion, resulting in a reduction in intrapulmonary pressure relative to atmospheric pressure. Intrapulmonary pressure thus becomes subatmospheric, establishing a pressure gradient from the upper to lower airways. As airflow progresses downward through the respiratory tract, encompassing the trachea, bronchi, and bronchioles, the pressure exhibits a gradual decline, aligning harmoniously with the increasing cross-sectional area observed in the lower airways. This explains the overarching trend of static surface pressure profiles following an anatomical sequence from top to bottom.

3.6. Vortices

In the human respiratory tract, characterized by a complex mixture of internal structures, constrictions, and expanses, turbulence is a well-founded phenomenon. As depicted in Fig. 11 (a), during the initial inhalation phase at 0.01 s, when air velocity remains low, a significant portion of velocity streamlines exhibits parallel alignment, indicative of laminar flow. However, a distinct vertex emerges beneath the vocal cords, marking the onset of turbulent flow. With the rapid surge in inflow velocity, reaching 50L/min by 0.05 s (as shown in Fig. 3), turbulent airflow intensifies, both in magnitude and spatial extent.

The impact of turbulent airflow, as seen in Fig. 11, is reflected in surface static temperature profiles, as showcased in Fig. 8 (c) and surface heat flux profiles in Fig. 9 (c), where G0 exhibits the lowest temperature and the highest heat flux among the lower airway regions. Similarly, the influence of turbulent airflow is evident in surface static temperature profiles found in Fig. 8 (b) and surface heat flux profiles within Fig. 9 (b), with the larynx exhibiting lower temperature and higher heat flux, ranking second only to the oral cavity among the upper airway segments.

The increased prevalence of turbulent flow significantly impacts local temperature distributions, subsequently influencing local surface heat flux. As illustrated in Fig. 12 (a to c), velocity streamlines at 0.06 s overlay velocity and temperature contours. Notably, specific regions feature vortices, mainly two located above the vocal cords on each side of the laryngopharynx and two below the vocal cords flanking the upper trachea. Cold air encounters these pre-existing vortices as it descends into the larynx region. The heightened velocity resulting from the vocal cord's constriction, coupled with the circular motion inherent to turbulent airflow, leads to increased cold air velocity and prolonged cold air-surface interaction. Consequently, this reduces wall surface temperature and a corresponding elevation in surface heat flux.

3.7. Further discussion and future studies

3.7.1. Clinical relevance

The study's insights into the thermal responses of the respiratory tract to cold air inhalation highlight the balance between heat transfer and airflow, which is crucial for maintaining the respiratory epithelium's function and integrity. These findings are relevant in the context of athletes training in cold environments, as the thermal and humidity balance within the airway is essential for protecting against airborne pathogens and particulate matter. This balance, as highlighted by the study's findings, is critical for preventing dryness, irritation, and subsequent inflammation of the respiratory tract, which can compromise mucociliary clearance and increase susceptibility to infections and thermal stress injuries. Previous studies on elite cross-country skiers

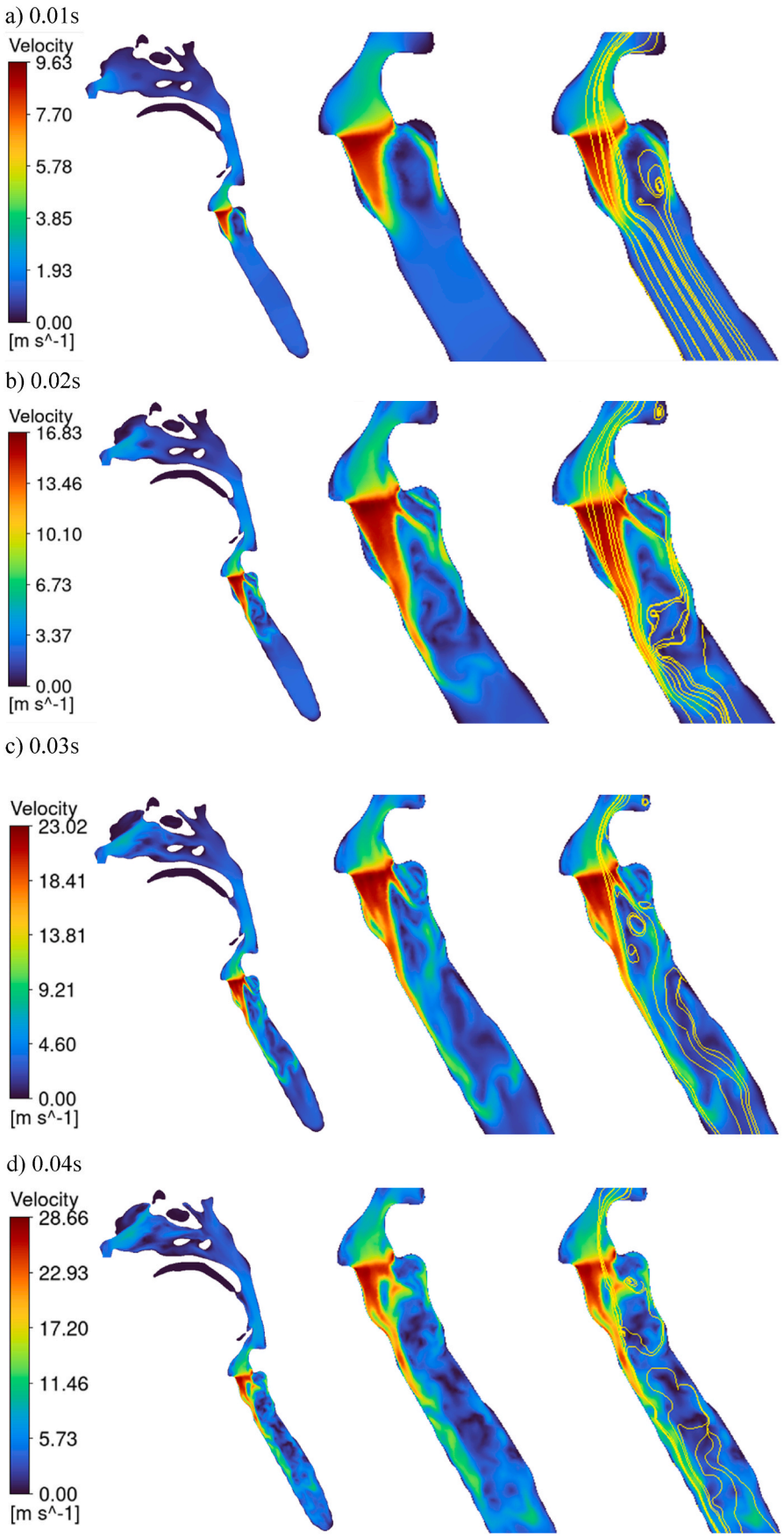

Fig. 11. Velocity contours in the central cross-sectional plane of the upper airway at (a) 0.01 s, (b) 0.02s, (c) 0.03s, and (d) 0.04 s, with enlarged views and velocity streamlines at the larynx and upper trachea region.

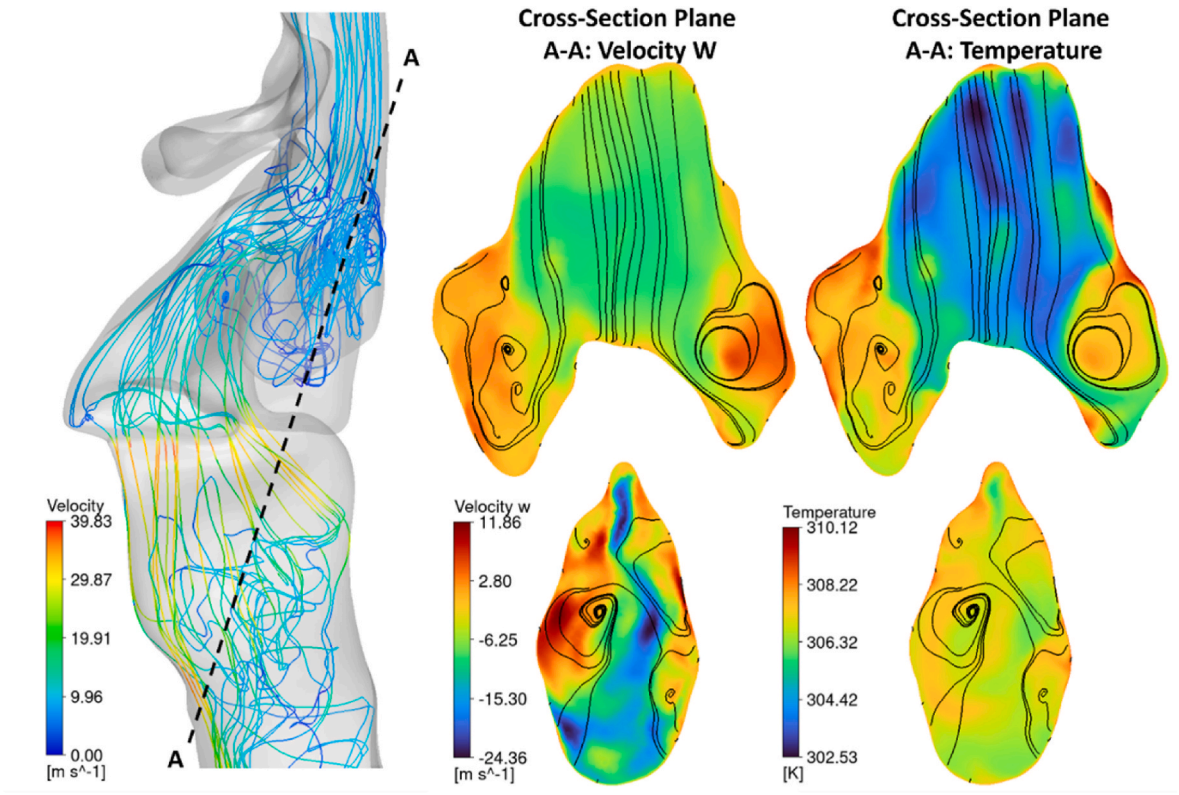

Fig. 12. Velocity streamlines at 0.06s, with (a) 3D streamlines at the larynx region, (b) 2D streamlines overlaid on velocity contour at a cross-sectional plane A-A, and (c) 2D streamlines overlaid on temperature contour.

further reinforce this notion, showing that these athletes exhibit indicators of chronic airway inflammation and damage to the airway epithelial lining [50–53].

Moreover, our findings resonate with existing literature emphasizing the adverse effects of environmental conditions on respiratory health. Research indicates that maintaining optimal humidity levels can mitigate dryness symptoms within the respiratory tract, thereby reducing the risk of irritation and the potential for compromised mucociliary clearance [54]. Dry air, however, impacts the balance of salt and water in the upper airways, thereby elevating the risk of respiratory diseases, including COVID-19 [55]. Furthermore, exposure to environmental pollutants, akin to the inhalation of cold and dry air, has been associated with increased respiratory symptoms, highlighting the importance of understanding and modeling these environmental impacts accurately [56].

3.7.2. *Elevation and air properties*

Elevation significantly influences air properties such as density and oxygen content. As elevation increases, the density of the air decreases systematically, which is also in proportion to the decrease in total pressure. This reduction in air density affects the body's ability to perform aerodynamic and respiratory functions effectively. For instance, at sea level, the density of air is about 1.21 kg/m^3, but at 4000 m elevation, it decreases to 0.74 kg/m^3, which represents a considerable reduction [57]. At higher altitudes, the partial pressure of oxygen within the lungs is significantly reduced. This decrease affects the oxygen gradient between the alveoli and blood, where oxygen is absorbed, and between the blood and tissues, where oxygen is released. As a result, the efficiency of oxygen transfer from the lungs to the blood and subsequently from the blood to the tissues is diminished [58]. Future research should delve into the effects of elevation on the respiratory system and examine its potential impacts on both health and performance in athletes.

3.7.3. *Inhalation modes*

Nasal breathing, as opposed to mouth breathing, has been associated with a number of physiological benefits that can influence athletic performance. Research [59] conducted on physically active individuals assessed the impact of distinct breathing strategies (nasal, oral, and combined) on short-term muscular endurance. Although no significant disparities were observed in overall repetitions to failure in resistance activities like the bench press across breathing modalities, nasal breathing was associated with significant physiological variations, such as heart rate and blood oxygen saturation levels. Supporting their view, additional evidence from a different investigation [60] provides empirical evidence indicating that the differences in performance metrics associated with the Wingate Anaerobic Cycle Test were minimal between modes of breathing. suggests that performance measures in the Wingate Anaerobic Cycle Test show negligible differences between breathing methods. Contrarily, another analysis [61] indicates that oral breathing facilitates greater air volume transfer, meeting the respiratory and metabolic demands of high-intensity exercises more effectively than nasal breathing. However, at lower exercise intensities, the benefits of nasal breathing, such as the inhalation of cleaner air and the reduction in respiration rates, might become more advantageous. The ability of nasal breathing to reduce symptoms of exercise-induced asthma, even if it might lower peak aerobic performance, shows how closely health, body processes, and achieving top performance in sports are connected.

The current study has successfully modeled scenarios of nasal breathing, offering substantial insights into the heat transfer within the respiratory tract. However, to foster a comprehensive understanding of respiratory heat transfer mechanisms, future research should extend to include scenarios of oral breathing.

3.7.4. *Latent heat transfer*

Incorporating into our discussion the importance of modeling latent heat transfer at airway wall surfaces, it becomes apparent that this

aspect is crucial in understanding health risks associated with airway heat exchange. Latent heat transfer, particularly through the process of moisture evaporation from the airway walls, impacts the local thermal environment and the body's response to inhaled air. This mechanism can alter the humidity and temperature of the air reaching the deeper lung regions, affecting mucosal function, and potentially exacerbating or mitigating respiratory conditions. The inclusion of latent heat transfer models in future studies can enhance the realism and applicability of simulations, providing better insights into the physiological impacts of various environmental conditions on respiratory health.

3.7.5. Computational usage

The present study utilized a computationally intensive modeling approach. Parallel computing was conducted using 62 cores across two CPUs (AMD EPYC 7532 2.40 GHz), with each simulation requiring over 770 h (32 days). This resulted in a total CPU core time of 95,782 h approximately.

4. Conclusion

A comprehensive investigation was undertaken into the dynamic mechanisms of heat transport within a 3D model of the human respiratory system, spanning from the nasal airways to the distal lung generations. The primary goal was to evaluate the heat transfer capacity within the human lung by employing Large Eddy Simulation in conjunction with an algebraic Wall-Modeled LES Sub-Grid Scale model. The principal findings of this extensive numerical analysis can be succinctly summarized as follows.

1. A highly dynamic temperature distribution pattern was observed along the airway wall during inhalation. This pattern featured a rapid initial temperature decline, succeeded by a subsequent increase, resulting in a 'U-shaped' temperature profile. The surface heat flux profile closely mirrored the temperature dynamics, exhibiting a substantial initial reduction in heat transfer, followed by a peak and subsequent decrease, resulting in an n-shaped heat flux profile.
2. The Nusselt number decreases with advancing airway generations, indicating a decrease in convective heat transfer efficiency in smaller airways. Inhalation of air at 5 °C consistently results in higher Nusselt numbers across all generations compared to 25 °C, highlighting the influence of a larger temperature gradient on heat transfer enhancement.
3. Notably, the upper airway displayed distinctive oscillatory and elevated static pressure patterns, while the lower airway maintained a consistent, subdued static pressure throughout the inhalation process.
4. Despite occasional deviations, the surface temperature, heat flux, and static pressure within the airway wall predominantly adhered to an anatomical sequence, demonstrating remarkable coherence from head to toe. Deviations from this order were attributed to the complex geometric features of the airway.
5. Of paramount significance was the role of turbulent airflow, particularly in the larynx and upper trachea region, which profoundly influenced local temperature, heat flux, and pressure distributions. Turbulent flow was associated with reduced wall surface temperature, increased heat flux, and decreased area-weighted wall static pressure in these regions.

These findings provide insights into the fluid and thermodynamics governing the response of the human airway to the inhalation of cold air. The observed temperature, heat flux, and pressure profiles hold significant implications for understanding how the airway responds to varying environmental conditions, with relevance for clinical and physiological contexts.

Nomenclature

d_w	wall distance (m)
h	convective heat transfer coefficient ($Wm^{-2}K^{-1}$)
h_j	enthalpy of species j (J)
$\boldsymbol{g}$	gravitational acceleration in the negative z-direction (ms^{-2})
k	turbulent kinetic energy (m^2s^{-2})
k_{air}	thermal conductivity of the air ($Wm^{-1}K^{-1}$)
k_{eff}	effective conductivity (m^2s^{-2})
p	static pressure (Pa)
t	time (s)
$\boldsymbol{u}$	fluid velocity vector (ms^{-1})
y^+	normal to the wall inner scaling
C_{Smag}	Model constant, which equals 0.2
E	energy (J)
$\boldsymbol{J}_j$	diffusion flux of species j
L	characteristic length, which is the radius of the airway (m)
Nu	Nusselt number
Q	surface heat flux (Wm^{-2})
S	strain rate (s^{-1})
T	the absolute temperature of the fluid (K)
ΔT	the wall-air temperature difference (K)
κ	model constant, which equals 0.4187
υ_t	turbulence viscosity (Pa·s)
ρ	fluid density (kgm^{-3})
τ	stress tensor (Pa)
τ_{eff}	effective stress tensor (Pa)

CRediT authorship contribution statement

Xinlei Huang: Writing – original draft, Visualization, Validation, Software, Methodology, Investigation, Formal analysis, Data curation. **Isabella Francis:** Writing – review & editing, Visualization, Formal analysis. **Goutam Saha:** Writing – review & editing, Validation, Investigation. **Md. M. Rahman:** Writing – review & editing, Writing – original draft, Software, Investigation. **Suvash C. Saha:** Writing – review & editing, Supervision, Project administration, Conceptualization.

Declaration of competing interest

The authors declare that they have no known competing financial interests or personal relationships that could have appeared to influence the work reported in this paper.

Data availability

No data was used for the research described in the article.

Acknowledgments

The author acknowledges the computation resources provided by the High-Performance Computing facility of the University of Technology Sydney. The authors used AI-assisted technology (ChatGPT 4) for language editing and grammar checking.

References

[1] L. Jiang, E. Ng, A. Yeo, S. Wu, F. Pan, W. Yau, J. Chen, Y. Yang, A perspective on medical infrared imaging, J. Med. Eng. Technol. 29 (6) (2005) 257–267.
[2] M.N. Cramer, D. Gagnon, O. Laitano, C.G. Crandall, Human temperature regulation under heat stress in health, disease, and injury, Physiol. Rev. 102 (4) (2022) 1907–1989.
[3] F. Huang, Q. Zhu, X. Zhou, D. Gou, J. Yu, R. Li, Z. Tong, R. Yang, Role of CFD based in silico modelling in establishing an in vitro-in vivo correlation of aerosol deposition in the respiratory tract, Adv. Drug Deliv. Rev. 170 (2021) 369–385.
[4] W.H. Finlay, A.R. Martin, Recent advances in predictive understanding of respiratory tract deposition, J. Aerosol Med. Pulm. Drug Deliv. 21 (2) (2008) 189–206.
[5] X. Huang, L.M. Clemon, M.S. Islam, S.C. Saha, Optimization of fluid characteristics in the main nozzle of an air-jet loom, Textil. Res. J. 92 (3–4) (2022) 525–538.
[6] S.C. Saha, I. Francis, G. Saha, X. Huang, M.M. Molla, Hemodynamic insights into abdominal aortic aneurysms: bridging the knowledge gap for improved patient care, Fluids 9 (2) (2024) 50.

[7] H. Shamohammadi, S. Mehrabi, S. Sadrizadeh, M. Yaghoubi, O. Abouali, 3D numerical simulation of hot airflow in the human nasal cavity and trachea, Comput. Biol. Med. 147 (2022) 105702.
[8] B. Haut, A. Nonclercq, A. Buess, J. Rabineau, C. Rigaut, B. Sobac, Comprehensive analysis of heat and water exchanges in the human lungs, Front. Physiol. 12 (2021) 649497.
[9] T. Hildebrandt, W.J. Heppt, U. Kertzscher, L. Goubergrits, The concept of rhinorespiratory homeostasis—a new approach to nasal breathing, Facial Plast. Surg. 29 (2) (2013) 85–92.
[10] E. Moreddu, L. Meister, A. Dabadie, J.-M. Triglia, M. Médale, R. Nicollas, Numerical simulation of nasal airflows and thermal air modification in newborns, Med. Biol. Eng. Comput. 58 (2020) 307–317.
[11] M.M. Rahman, M. Zhao, M.S. Islam, K. Dong, S.C. Saha, Numerical study of nanoscale and microscale particle transport in realistic lung models with and without stenosis, Int. J. Multiphas. Flow 145 (2021) 103842.
[12] C. Croce, R. Fodil, M. Durand, G. Sbirlea-Apiou, G. Caillibotte, J.-F. Papon, J.-R. Blondeau, A. Coste, D. Isabey, B. Louis, In vitro experiments and numerical simulations of airflow in realistic nasal airway geometry, Ann. Biomed. Eng. 34 (2006) 997–1007.
[13] P.F. Walker, M.F. Buehner, L.A. Wood, N.L. Boyer, I.R. Driscoll, J.B. Lundy, L. C. Cancio, K.K. Chung, Diagnosis and management of inhalation injury: an updated review, Crit. Care 19 (1) (2015) 1–12.
[14] D.J. Dries, F.W. Endorf, Inhalation injury: epidemiology, pathology, treatment strategies, Scand. J. Trauma Resuscitation Emerg. Med. 21 (2013) 1–15.
[15] H.G. Hanstock, M. Ainegren, N. Stenfors, Exercise in sub-zero temperatures and airway health: implications for athletes with special focus on heat-and-moisture-exchanging breathing devices, Frontiers in Sports and Active Living 2 (2020).
[16] P. Wohlsein, M. Peters, C. Schulze, W. Baumgärtner, Thermal injuries in veterinary forensic pathology, Veterinary pathology 53 (5) (2016) 1001–1017.
[17] E.F. Haponik, W.R. Summer, Respiratory complications in burned patients: pathogenesis and spectrum of inhalation injury, J. Crit. Care 2 (1) (1987) 49–74.
[18] B. Tsuji, Y. Chinda, Y. Honda, N. Fujii, N. Kondo, T. Nishiyasu, Effects of cold air inhalation on body temperature, respiratory and cerebrovascular responses during exercise in the heat, Extreme Physiol. Med. 4 (1) (2015) A128.
[19] T.M. Ikäheimo, Cardiovascular diseases, cold exposure and exercise, Temperature 5 (2) (2018) 123–146.
[20] H.O. Koskela, Cold air-provoked respiratory symptoms: the mechanisms and management, Int. J. Circumpolar Health 66 (2) (2007) 91–100.
[21] F. Brocherie, O. Girard, G.P. Millet, Emerging environmental and weather challenges in outdoor sports, Climate 3 (3) (2015) 492–521.
[22] C. Li, J. Jiang, H. Dong, K. Zhao, Computational modeling and validation of human nasal airflow under various breathing conditions, J. Biomech. 64 (2017) 59–68.
[23] M. Rahman, M. Zhao, M.S. Islam, K. Dong, S.C. Saha, Numerical study of nano and micro pollutant particle transport and deposition in realistic human lung airways, Powder Technol. 402 (2022) 117364.
[24] H. Gatterer, T. Dünnwald, R. Turner, R. Csapo, W. Schobersberger, M. Burtscher, M. Faulhaber, M.D. Kennedy, Practicing sport in cold environments: practical recommendations to improve sport performance and reduce negative health outcomes, Int. J. Environ. Res. Publ. Health 18 (18) (2021) 9700.
[25] B. Kingma, A. Frijns, W. van Marken Lichtenbelt, The thermoneutral zone: implications for metabolic studies, Frontiers in Bioscience-Elite 4 (5) (2012) 1975–1985.
[26] J. Oksa, M.B. Ducharme, H. Rintamaki, Combined effect of repetitive work and cold on muscle function and fatigue, J. Appl. Physiol. 92 (1) (2002) 354–361.
[27] J. Oksa, H. Rintamäki, S. Rissanen, Muscle performance and electromyogram activity of the lower leg muscles with different levels of cold exposure, Eur. J. Appl. Physiol. Occup. Physiol. 75 (1997) 484–490.
[28] U. Lindemann, J. Oksa, D.A. Skelton, N. Beyer, J. Klenk, J. Zscheile, C. Becker, Effect of cold indoor environment on physical performance of older women living in the community, Age Ageing 43 (4) (2014) 571–575.
[29] K. Phillips, B. Noh, M. Gage, T. Yoon, The effect of cold ambient temperatures on climbing-specific finger flexor performance, Eur. J. Sport Sci. 17 (7) (2017) 885–893.
[30] S. Saha, I. Francis, X. Huang, A. Paul, Heat transfer and fluid flow analysis of realistic 16-generation lung, Phys. Fluids 34 (2022).
[31] X. Huang, S.C. Saha, G. Saha, I. Francis, Z. Luo, Transport and deposition of microplastics and nanoplastics in the human respiratory tract, Environmental Advances 16 (2024) 100525.
[32] S.C. Saha, X. Huang, I. Francis, G. Saha, Airway stability in sleep apnea: assessing continuous positive airway pressure efficiency, Respir. Physiol. Neurobiol. 325 (2024) 104265.
[33] ANSYS, large eddy simulation (LES) model, in: I. ANSYS (Ed.), ANSYS Fluent Theory Guide, ANSYS, Inc., 2020, pp. 110–111, 2600 ANSYS Drive Canonsburg, PA 15317.
[34] ANSYS, Algebraic wall-modeled LES model (WMLES), in: I. ANSYS (Ed.), ANSYS Fluent Theory Guide, ANSYS, Inc., 2020, pp. 114–116, 2600 ANSYS Drive Canonsburg, PA 15317.
[35] ANSYS, subgrid-scale models, in: I. ANSYS (Ed.), ANSYS Fluent Theory Guide, ANSYS, Inc., 2020, pp. 111–112, 2600 ANSYS Drive Canonsburg, PA 15317.
[36] ANSYS, the mass conservation equation, in: I. ANSYS (Ed.), ANSYS Fluent Theory Guide, ANSYS, Inc., 2020, pp. 2–3, 2600 ANSYS Drive Canonsburg, PA 15317.
[37] ANSYS, Momentum conservation equations, in: I. ANSYS (Ed.), ANSYS Fluent Theory Guide, ANSYS, Inc., 2020, pp. 3–4, 2600 ANSYS Drive Canonsburg, PA 15317.
[38] ANSYS, the energy equation, in: A. Inc (Ed.), ANSYS Fluent Theory Guide, ANSYS, Inc., 2020, p. 150, 2600 ANSYS Drive Canonsburg, PA 15317.
[39] B. Kumar, V. Srivastav, A. Jain, A. Paul, Study of Numerical Schemes for the CFD Simulation of Human Airways, 2019, pp. 32–40.
[40] J. Wedel, P. Steinmann, M. Štrakl, M. Hriberšek, Y. Cui, J. Ravnik, Anatomy matters: the role of the subject-specific respiratory tract on aerosol deposition - a CFD study, Comput. Methods Appl. Mech. Eng. 401 (2022) 115372.
[41] E.G. Chekan, J.F. Cummings, I. Mabe, S. Hunter, J.W. Clymer, Thickness of cadaveric human lung tissue, Surg. Technol. Int. 29 (2016) 207–213.
[42] D. Yang, M. Cao, Effect of changes in lung physical properties on microwave ablation zone during respiration, Biomed Eng Lett 10 (2) (2020) 285–298.
[43] J. Van Dyk, T.J. Keane, W.D. Rider, Lung density as measured by computerized tomography: implications for radiotherapy, Int. J. Radiat. Oncol. Biol. Phys. 8 (8) (1982) 1363–1372.
[44] K. Liener, J. Durr, R. Leiacker, A. Rozsasi, T. Keck, Measurement of tracheal humidity and temperature, Respiration 73 (3) (2006) 324–328.
[45] B. Cohen, R. Sussman, M. Lippmann, Ultrafine particle deposition in a human tracheobronchial cast, Aerosol Science and Technology - AEROSOL SCI TECH 12 (1990) 1082–1091.
[46] K. Horsfield, G. Dart, D.E. Olson, G.F. Filley, G. Cumming, Models of the human bronchial tree, J. Appl. Physiol. 31 (2) (1971) 207–217.
[47] M.S. Islam, S.C. Saha, E. Sauret, T. Gemci, Y.T. Gu, Pulmonary aerosol transport and deposition analysis in upper 17 generations of the human respiratory tract, J. Aerosol Sci. 108 (2017) 29–43.
[48] B. Haut, A. Nonclercq, A. Buess, J. Rabineau, C. Rigaut, B. Sobac, Comprehensive analysis of heat and water exchanges in the human lungs, Front. Physiol. 12 (2021) 649497.
[49] Chapter 2 Morphometry of the human respiratory system, in: C.-s. Wang (Ed.), Interface Science and Technology, Elsevier, 2005, pp. 7–30.
[50] E.M. Karjalainen, A. Laitinen, M. Sue-Chu, A. Altraja, L. Bjermer, L.A. Laitinen, Evidence of airway inflammation and remodeling in ski athletes with and without bronchial hyperresponsiveness to methacholine, Am. J. Respir. Crit. Care Med. 161 (6) (2000) 2086–2091.
[51] S.-C. Malcolm, Winter sports athletes: long-term effects of cold air exposure, Br. J. Sports Med. 46 (6) (2012) 397.
[52] M. Sue-Chu, E.M. Karjalainen, A. Altraja, A. Laitinen, L.A. Laitinen, A.B. Naess, L. Larsson, L. Bjermer, Lymphoid aggregates in endobronchial biopsies from young elite cross-country skiers, Am. J. Respir. Crit. Care Med. 158 (2) (1998) 597–601.
[53] M. Sue-Chu, L. Larsson, T. Moen, S. Rennard, L. Bjermer, Bronchoscopy and bronchoalveolar lavage findings in cross-country skiers with and without "ski asthma", Eur. Respir. J. 13 (3) (1999) 626–632.
[54] K. Byber, T. Radtke, D. Norbäck, C. Hitzke, D. Imo, M. Schwenkglenks, M.A. Puhan, H. Dressel, M. Mutsch, Humidification of indoor air for preventing or reducing dryness symptoms or upper respiratory infections in educational settings and at the workplace, Cochrane Database Syst. Rev. 12 (12) (2021) Cd012219.
[55] R.D. Field, N. Moelis, J. Salzman, A. Bax, D. Ausiello, S.M. Woodward, X. Wu, F. Dominici, D.A. Edwards, Inhaled water and salt suppress respiratory droplet generation and COVID-19 incidence and death on US coastlines, Molecular Frontiers Journal 5 (01n02) (2021) 17–29.
[56] J. McLean, D. Anderson, G. Capra, C.A. Riley, The potential effects of burn pit exposure on the respiratory tract: a systematic review, Mil. Med. 186 (7–8) (2021) 672–681.
[57] D.L. Altshuler, R. Dudley, The physiology and biomechanics of avian flight at high altitude, Integr. Comp. Biol. 46 (1) (2006) 62–71.
[58] W.L. Kenney, J.H. Wilmore, D.L. Costill, Physiology of Sport and Exercise, Human kinetics, 2021.
[59] F. Lörinczi, M. Vanderka, D. Lörinczová, M. Kushkestani, Nose vs. mouth breathing– acute effect of different breathing regimens on muscular endurance, BMC Sports Science, Medicine and Rehabilitation 16 (1) (2024) 42.
[60] C. Recinto, T. Efthemeou, P.T. Boffelli, J.W. Navalta, Effects of nasal or oral breathing on anaerobic power output and metabolic responses, Int J Exerc Sci 10 (4) (2017) 506–514.
[61] C.O. LaComb, in: Oral vs. Nasal Breathing during Submaximal Aerobic Exercise, 2015.